nature chemistry

Article

https://doi.org/10.1038/s41557-026-02161-2

Blocking oxidation of α-hydrogens enables non-fluorinated solvents to achieve high-potential stability in lithium batteries

Received: 21 October 2025

Accepted: 22 April 2026

Published online: 26 May 2026

Check for updates

Yu-Xin Huang[1,10], Yi Yang[2,10], Chen-Zi Zhao[1,3] ✉, Pan Xu[1,4,5], Zi-Yue Jiang[1], Zi-Zhang Qiu[1], Xing-Yu Zhong[1], Zong-Yao Shuang[1], Xue-Yan Huang[1], Yong-Feng Li[1], Wei-Jin Kong[1], Yi-Fan Tan[6], Xiang Chen[1], Kaihang Zhang[7], Jia-Qi Huang[2] & Qiang Zhang[1,3,8,9] ✉

Developing next-generation batteries that are high-energy, low-cost and eco-friendly is crucial for industrial applications. Lithium-rich manganese-based oxide positive electrodes offer substantial specific energy, enabled by their high specific capacity at high charging potential (>4.6 V versus Li/Li$^+$). However, stable operation at such high potentials remains challenging, as most electrolytes rely on environmentally unfriendly fluorinated solvents. Here we identified α-oxidation of the carbonyl group as the main oxidation mechanism of carboxylate esters. By removing all the reactive α-hydrogens of methyl acetate, we demonstrate that methyl trimethylacetate is a non-fluorinated, high-potential-stable solvent. This solvent exhibits outstanding oxidative stability up to 5.6 V versus Li/Li$^+$, and electrochemical cells using methyl-trimethylacetate-based electrolytes maintain stable cycling at 4.6/4.7 V, outperforming many fluorinated systems. An industrial-scale 7.2-Ah pouch cell reached a maximum specific energy of 652.4 Wh kg^{-1} with 94.5% capacity retention after 28 cycles at 0.1 C/0.2 C. This work provides a simple molecular design strategy that addresses specific energy, cost and sustainability in next-generation high-voltage lithium batteries.

High-voltage lithium batteries are widely regarded as a key technology for next-generation energy storage because they offer the potential to break through the specific energy limits of conventional lithium-ion systems. Operating at voltages above 4.4 V enables specific energies exceeding 600 Wh kg^{-1} in lithium metal batteries (LMBs), which are critical for electric vehicles and electric aviation[1]. To achieve such high performance, positive electrode (positrode) materials capable of delivering both high-potential (≥4.4 V versus Li/Li$^+$) and high-capacity (≥200 mAh g^{-1}) are essential. Among the candidates, lithium-rich manganese oxide ($Li_{1.2}Mn_{0.54}Co_{0.13}Ni_{0.13}O_2$, LRMO) positrode is of particular interest because it combines a high cutoff voltage above 4.6 V in LMBs and a capacity exceeding 250 mAh g^{-1} with the advantages of low cost and reduced toxicity[2,3].

Despite this potential, stable operation of high-voltage lithium batteries is fundamentally constrained by electrolytes. Conventional non-fluorinated solvents such as carbonates[4], ethers[5,6], siloxanes[7,8] and phosphates[9,10] typically undergo oxidative decomposition above 4.4 V versus Li/Li$^+$, resulting in a short cycle life[11]. To overcome this issue, highly concentrated electrolytes and localized highly concentrated electrolytes (LHCEs) have been proposed[12,13], which improve stability by reducing the number of free solvent molecules. More recently, fluorinated electrolytes have been introduced[14]; in these, the strong electron-withdrawing effect of fluorine lowers the highest occupied molecular orbital (HOMO) levels of solvents, thereby enhancing their oxidative stability.

However, the widespread adoption of these approaches faces critical barriers. The high Li-salt consumption in HCEs and the reliance

A full list of affiliations appears at the end of the paper. ✉e-mail: zcz@mail.tsinghua.edu.cn; zhang-qiang@mails.tsinghua.edu.cn

https://doi.org/10.1038/s41557-026-02161-2

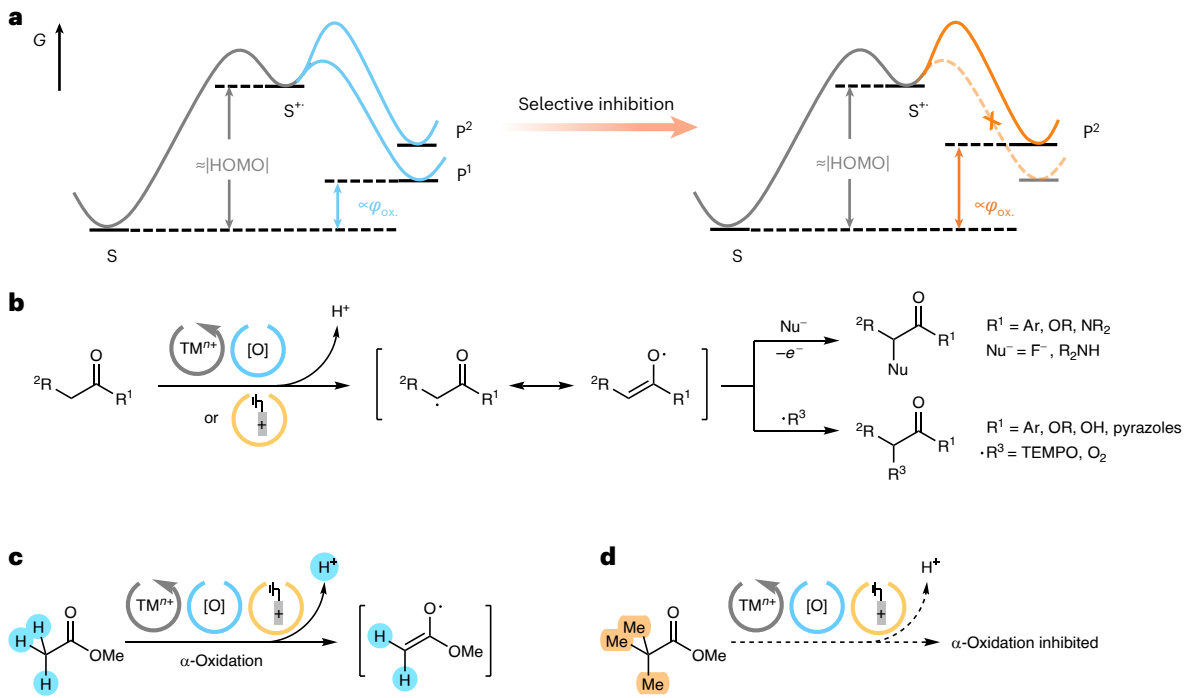

Fig. 1 | The design principle of non-fluorinated, high-potential-stable solvent MTMA. a, General oxidation mechanism of a solvent molecule S and a possible way to raise its high-potential stability. **b**, Common α-oxidation reactions of carbonyl compounds. **c**, The proposed oxidation mechanism of MA with high-potential positrode in lithium batteries. **d**, Suppression of α-oxidation in MTMA as no α-hydrogen is present. Ox., oxidation; [O], oxidant.

on fluorinated solvents in LHCEs and fluorinated electrolytes lead to prohibitively high costs[12,15]. Many fluorinated solvents and diluents fall in the category of per- and polyfluoroalkyl substances (PFAS), which are bioaccumulative and subject to growing regulatory restrictions[15,16]. Even partially fluorinated solvents not classified in this way, such as fluoroethylene carbonate (FEC), can generate hazardous byproducts (for example, HF and fluorides) upon degradation[15,17]. Therefore, to successfully commercialize high-specific-energy batteries, it is vital to develop a new class of cost-effective and environmentally friendly electrolytes compatible with high-potential positrodes and Li metal negative electrodes (negatrodes).

Here we propose that a low HOMO is not a prerequisite for high anodic stability, provided that the dominant oxidation pathway can be selectively blocked. We first select carboxylate esters for verification because their oxidation chemistry has been relatively well established in organic chemistry. We aim to identify their primary decomposition mechanism in high-voltage LMBs and remove the vulnerable molecular sites to achieve high anodic stability without using electron-withdrawing groups. Specifically, as α-oxidation of carbonyls is common in organic chemistry, we substitute the reactive α-hydrogens of a carboxylate with inert methyl groups, yielding methyl trimethylacetate (MTMA). We then evaluate whether this non-fluorinated solvent achieves high anodic stability in practical LMBs. Finally, we explore the broader applicability of this strategy in other solvents prone to α-oxidation—including amides, ketones and ethers—to assess it as a general approach for development of non-fluorinated high-potential-stable electrolytes.

Results and discussion

Molecular design of MTMA

To design a high-potential-stable solvent without fluorine or other electron-withdrawing groups, we first re-evaluated the rationale of the conventional fluorination strategy. Fluorination typically enhances anodic stability by lowering the HOMO energy level. According to Koopmans' theorem[18,19], this increases the first ionization energy of the solvent, theoretically hindering the initial electron transfer to the positrode. However, radical cations generated after this initial ionization of small solvent molecules are usually highly unstable[20]. As these transient intermediates rapidly decompose into more stable products, the applied potential does not need to match the large first ionization energy to drive solvent oxidation[21]. Instead, the thermodynamic oxidation potential is dictated by the Gibbs energy difference between the solvent and its final oxidation product, largely independent of the HOMO energy level and first ionization energy[22].

As discussed, the HOMO energy level of a solvent molecule, denoted S, does not necessarily determine its oxidation potential (Fig. 1a). The unstable radical cation $S^{+\cdot}$ rapidly decomposes into stable intermediates or final products (P^1 and P^2). Theoretically, the Gibbs energy difference between S and its most stable product (P^1) is proportional to the thermodynamic oxidation potential of S. By selectively blocking the least endergonic pathway to P^1, we can redirect the solvent molecule towards its less favourable product P^2. Therefore, we can raise the thermodynamic oxidation potential of S without lowering its HOMO energy level. Similarly, we can increase the activation overpotential and kinetically inhibit oxidation by redirecting S towards the first stable intermediate of higher energy.

We first chose carbonyl compounds to test our molecular design strategy, because many common lithium battery solvents—including carbonate esters, carboxylate esters, amides and ketones—contain this functional group. In organic chemistry, α-oxidation is a prevalent reaction pathway for carbonyls[23] (Fig. 1b). The reaction mechanism and conditions of the α-oxidation is discussed in Supplementary Note 1. Notably, high-potential positrodes such as LRMO and nickel-rich $LiNi_xCo_yMn_{1-x-y}O_2$ (NCM) simultaneously provide all the reaction conditions required for α-oxidation: they contain catalytic transition metal ions (Mn, Co, Ni), active oxidants (high-valent Mn, Co, Ni and O^{n-} in Li-rich positrodes, $0 \le n < 2$) and the anodic driving force during charging. Therefore, we conjectured that carbonyl compounds with carbonyl α-hydrogens would undergo α-oxidation as the major side reaction in these batteries.

https://doi.org/10.1038/s41557-026-02161-2

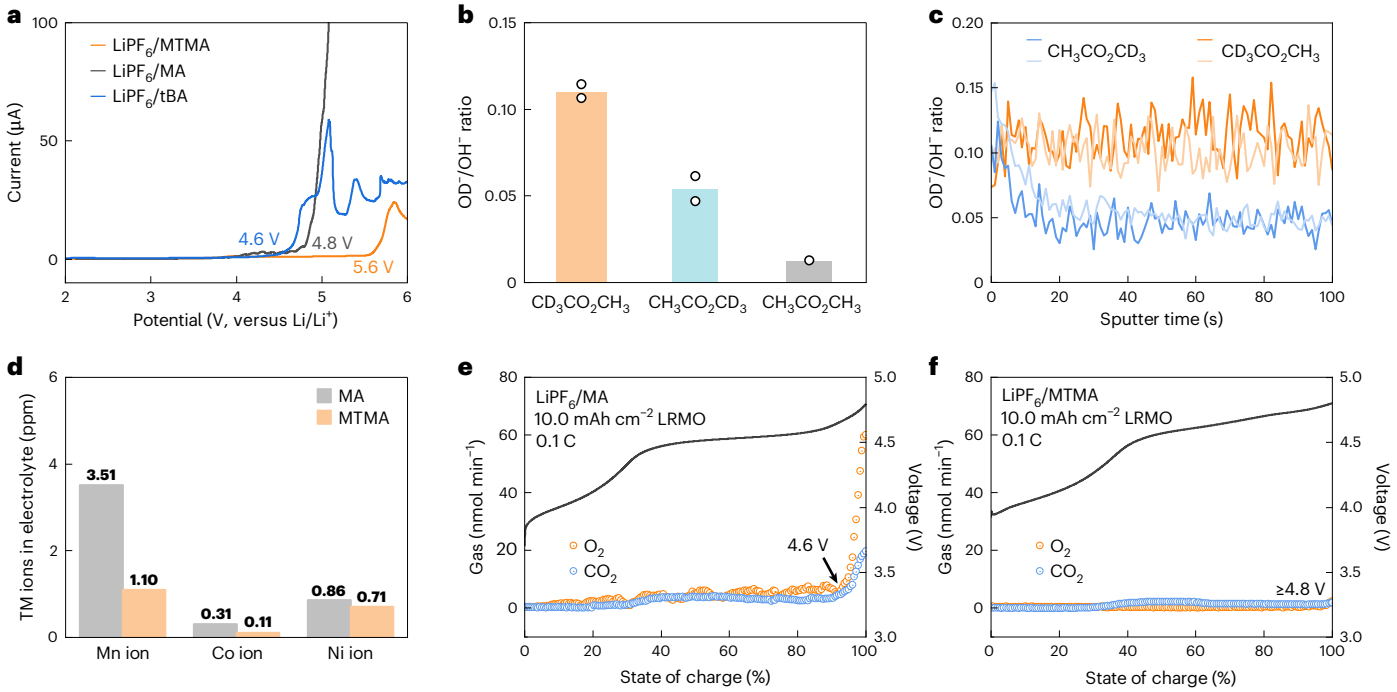

Fig. 2 | Characterization of MA oxidation mechanism. a, LSV anodic scanning of MTMA, MA and *t*-butyl acetate electrolytes. **b**, Total OD^-/OH^- ratio of the surface of LRMO positrodes charged in different deuterated MA electrolytes. Two parallel samples using each deuterated MA were measured. **c**, Depth profile of OD^-/OH^- ratio of the surface of LRMO positrodes charged in different MA electrolytes. Two parallel samples using each deuterated MA were measured. **d**, Concentrations of dissolved transition metal (TM) ions in MA and MTMA electrolytes after LSV scanning using LRMO positrode in an H-cell. **e**,**f**, DEMS experiments using MA (**e**) and MTMA (**f**) electrolytes. tBA, *t*-butyl acetate.

To isolate and verify this mechanism, we required a simple model solvent. Carbonate esters lack carbonyl α-hydrogens and undergo complex, parallel oxidation pathways (for example, C–O bond cleavage[24,25], ethereal α-hydrogen abstraction[26] and insertion[27]), making them unsuitable. Hence, we chose methyl acetate (MA; structure shown in Fig. 1c and Supplementary Fig. 1) as our model solvent. To block the potential α-oxidation of MA, all its carbonyl α-hydrogens were replaced with inert methyl groups, yielding MTMA (structure shown in Fig. 1d and Supplementary Fig. 1) as our non-fluorinated, high-potential-stable solvent.

MA oxidation mechanism and MTMA design validation

To confirm that α-oxidation was the primary oxidation pathway for MA, we conducted linear sweep voltammetry (LSV) using 1.0 M $LiPF_6$. MA oxidized at 4.8 V versus Li/Li^+ on a carbon-coated aluminium electrode, which may have become insufficient for actual positrodes such as LRMO[28] (Fig. 2a). Removal of the α-hydrogens of MA substantially improved its anodic stability, with MTMA resisting oxidation up to 5.6 V versus Li/Li^+. Conversely, *t*-butyl acetate, which lacks ethereal hydrogens but retains α-hydrogens, oxidized similarly to MA. In completely fluorine-free formulations with 1.0 M $LiClO_4$, the same phenomenon was observed (Supplementary Fig. 2 and Supplementary Note 2). This confirmed that ethereal hydrogen deprotonation is negligible, and α-oxidation dominates in carboxylates. Notably, $LiPF_6$/MTMA outperformed state-of-the-art all-fluorinated electrolyte LB372 (refs. 29,30; formulation in Methods), which is only stable up to 4.9 V versus Li/Li^+ (Supplementary Fig. 3). Furthermore, when evaluated in Li/LRMO cells at 4.8 V, $LiPF_6$/MTMA exhibited a lower leak current compared with $LiPF_6$/MA and LB372 (Supplementary Fig. 4); this finding validated our molecular design on actual positrodes.

To directly track this α-oxidation on the LRMO positrode, we charged cells in two partially deuterated MA electrolytes ($CD_3CO_2CH_3$ and $CH_3CO_2CD_3$; Supplementary Fig. 5 and Supplementary Note 3). Time-of-flight secondary ion mass spectrometry (TOF-SIMS) revealed that the LRMO surface OD^- content was consistently higher with $CD_3CO_2CH_3$, confirming that the positrode was primarily protonated by the carbonyl α-hydrogens (Fig. 2b,c). Density functional theory (DFT) calculations further supported this, showing that α-C–H bond cleavage was the most thermodynamically favourable decomposition route for the MA radical cation (Supplementary Fig. 6).

Understanding downstream oxidation products is critical, as these dictate positrode electrolyte interphase (PEI) stability and long-term cycling. Therefore, we further studied the oxidation products of MA to elucidate its complete oxidation mechanism on LRMO positrodes. Positrode protonation caused by solvent deprotonation is known to cause dissolution of transition metals; hence, the concentrations of dissoluted metals were measured. Indeed, H-cell measurements (Supplementary Fig. 7) after 4.8 V charging showed roughly triple the dissolved Mn and Co ions in $LiPF_6$/MA (3.51 and 0.31 ppm, respectively) compared with $LiPF_6$/MTMA (1.10 and 0.11 ppm, respectively) (Fig. 2d). This severe α-oxidation produced abundant protons that converted LRMO surface O^{2-} to OH^- and generated free H_2O. Karl Fischer titration confirmed a 20.8 ppm H_2O surge in $LiPF_6$/MA, whereas H_2O concentration remained largely unchanged in $LiPF_6$/MTMA (Supplementary Fig. 8). This generated water hydrolysed PF_6^- into detrimental HF and $PO_2F_2^-$ (Supplementary Figs. 9 and 10). Moreover, approximately 2 ppm of dissolved peroxides were detected in $LiPF_6$/MA after soaking with charged LRMO positrode, whereas none was present in $LiPF_6$/MTMA (Supplementary Fig. 11). This suggests that surface peroxy/superoxy species of the charged LRMO positrode bond with the MA α-radical to form soluble organic peroxides in the electrolyte. Furthermore, differential electrochemical mass spectrometry (DEMS) detected substantial CO_2 and O_2 release in MA starting at 4.6 V (Fig. 2e), whereas gas evolution was largely suppressed in MTMA (Fig. 2f) and LB372 (Supplementary Fig. 12) before 4.8 V. Finally, insoluble organics also formed during MA oxidation and constituted major components

https://doi.org/10.1038/s41557-026-02161-2

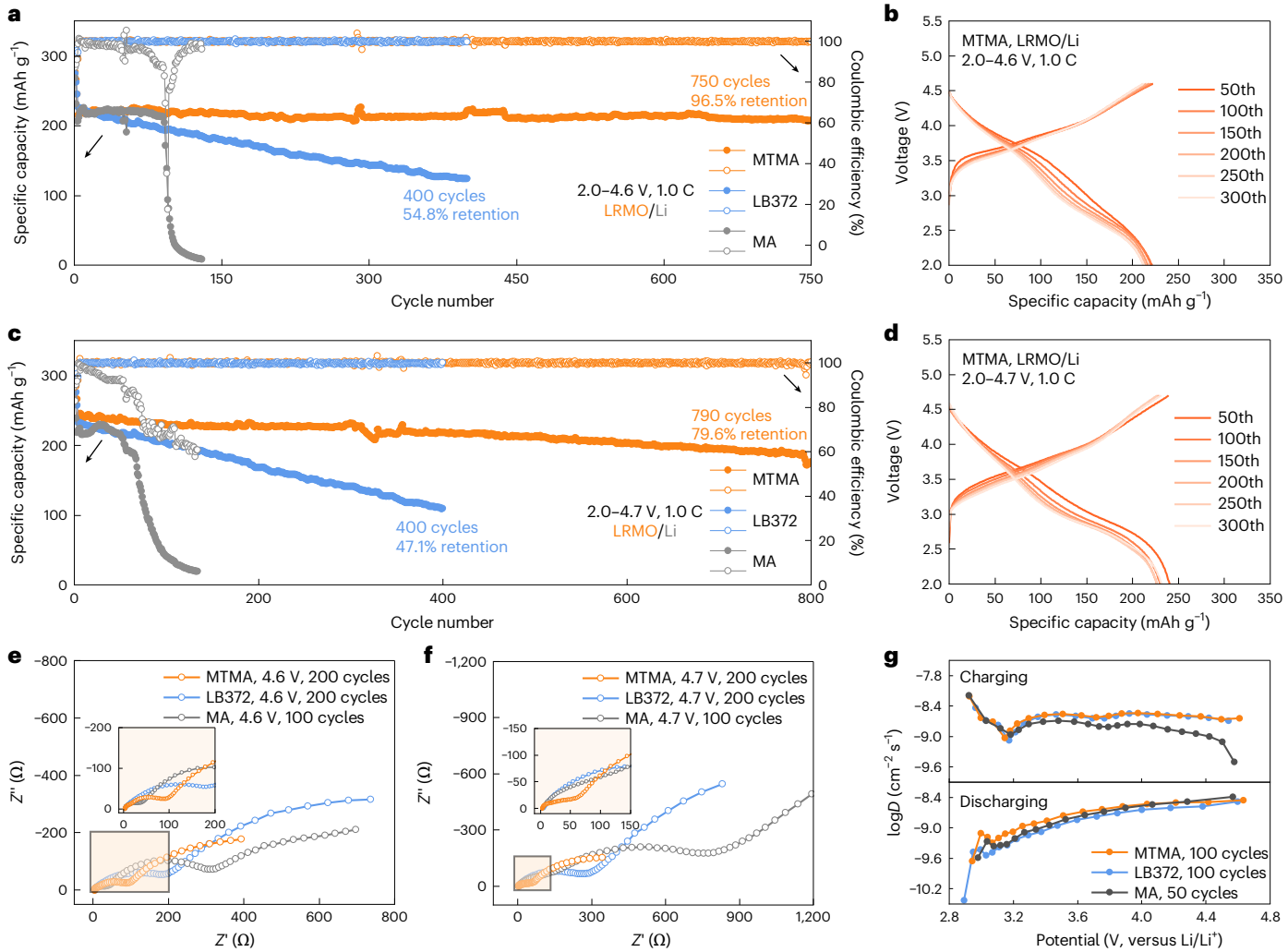

Fig. 3 | Cycling performance and electrochemical characterization of different electrolytes in low-loading LRMO coin cells. a, Cycling performance of 4.6 V Li/LRMO cells. **b**, Charge/discharge profiles of 4.6 V Li/LRMO cell using MTMA electrolyte. **c**, Cycling performance of 4.7 V Li/LRMO cells. **d**, Charge/discharge profiles of 4.7 V Li/LRMO cell using MTMA electrolyte. **e**,**f**, EIS spectra of Li/LRMO cells with different electrolytes at charging cutoff voltage of 4.6 V (**e**) and 4.7 V (**f**). **g**, Galvanostatic intermittent titration technique results for cycled Li/LRMO cells in different electrolytes.

of the PEI. On the basis of these results, we proposed a complete mechanism of MA oxidation on the LRMO positrode, initiated by oxidation at the carbonyl α-position (Supplementary Fig. 13). By removing all α-hydrogens, MTMA effectively inhibits this cascading generation of transition metal ions, H_2O, HF, CO_2 and O_2 gases, ensuring stable Li/LRMO cycling.

To develop a MTMA-based electrolyte that was compatible with both Li metal and LRMO, we formulated 1.2 M LiFSI + 0.4 M LiDFOB in MTMA as our non-fluorinated, high-potential-stable electrolyte for LMBs, with MA (same solutes) and LB372 electrolytes as comparisons. To exclude the effect of the Li negatrode and assess the 'intrinsic' performance of the LRMO positrode with different electrolytes, we used a large excess of Li negatrode (0.5 mAh cm^{-2} LRMO positrode paired with 600 μm Li negatrode)[31]. The cell with MTMA electrolyte achieved 96.5% capacity retention after 750 cycles at 1.0 C charge/discharge between 2.0 and 4.6 V (Fig. 3a,b). Despite being highly fluorinated, the cell with LB372 maintained only 54.8% of its initial capacity after 400 cycles. The capacity of the MA-based cell plummeted after ~100 cycles owing to the severe α-oxidation reaction. Even under a harsher 4.7-V cutoff, MTMA showed 79.6% retention over 790 cycles, whereas that of LB372 degraded to 47.1% within 400 cycles (Fig. 3c,d). Li/LRMO cells cycled with MTMA showed lower impedance compared with those with MA and LB372 (Fig. 3e,f); this was attributed to suppression of side reactions that thicken the PEI and/or solid electrolyte interphase (SEI) on the Li negatrode. In situ electrochemical impedance spectroscopy (EIS) measurements also suggested that thinner and more conductive interphases were formed in cycled MTMA cells, compared with cycled LB372 and MA cells (Supplementary Figs. 14–16). Owing to fewer interfacial side reactions, MTMA also gave a higher Li^+ diffusion coefficient in the cycled LRMO positrode compared with MA and LB372 (Fig. 3g). These results validate our design and demonstrate that rationally designed non-fluorinated electrolytes can match and outperform state-of-the-art fluorinated alternatives.

Characterization of PEI and LRMO positrodes

Compared with conventional layered positrode materials such as NCM, highly oxidative LRMO positrodes face more severe stability challenges, including irreversible phase transitions, lattice oxygen loss, transition metal dissolution, stress-induced particle cracking and interfacial side reactions with the electrolyte[32]. As bulk structure degradation is known to initiate at the surface before propagating inward[31,33], formation of a stable PEI is important for long-term durability.

Accordingly, we used X-ray photoelectron spectroscopy to characterize the chemical composition of the PEIs derived from different

https://doi.org/10.1038/s41557-026-02161-2

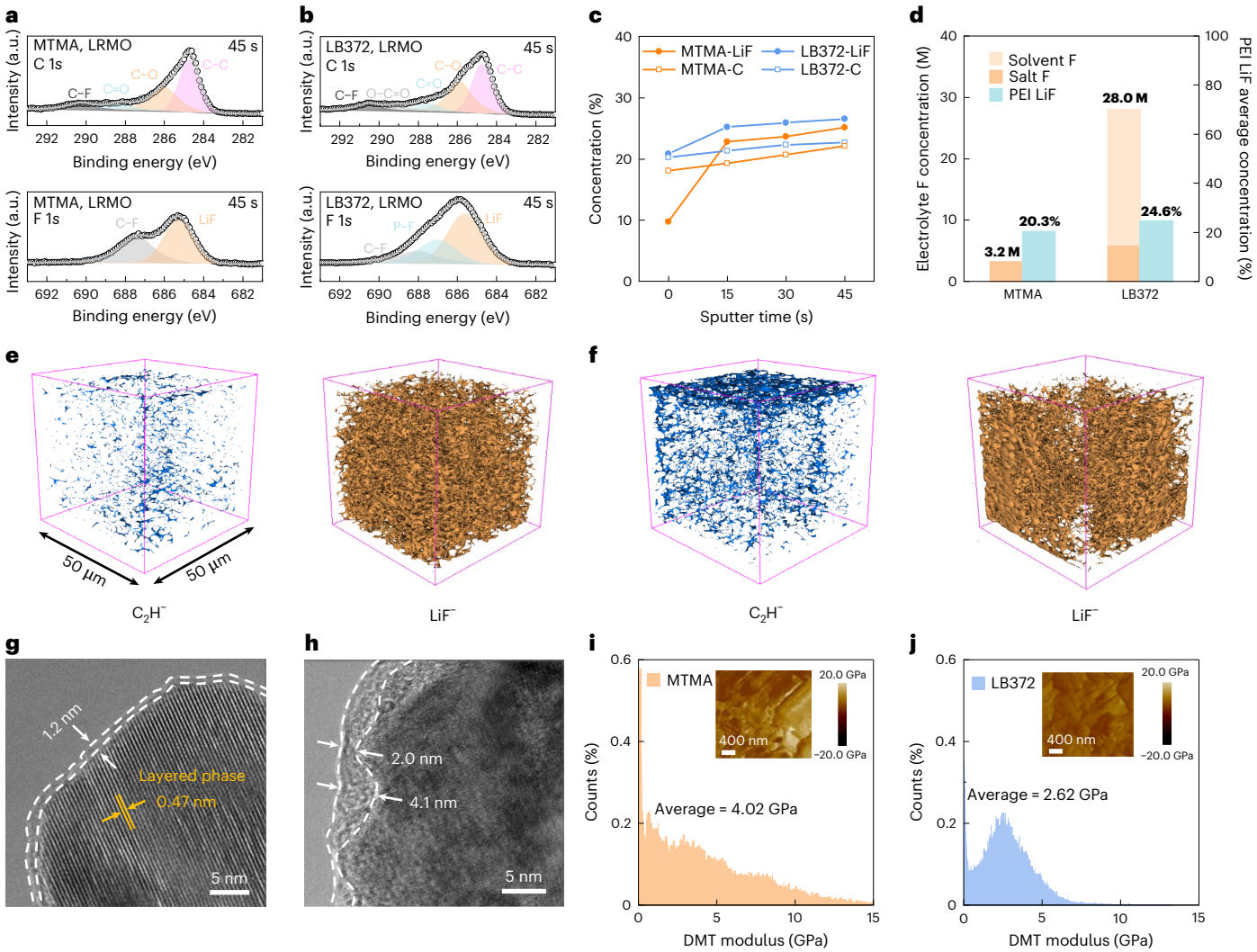

Fig. 4 | The characterizations of LRMO PEIs. a,**b**, F 1*s* and C 1*s* X-ray photoelectron spectroscopy spectra of LRMO PEIs after 100 cycles in MTMA (**a**) and LB372 (**b**). **c**, LiF and total carbon concentration in PEIs at various sputtering times. **d**, Comparison of electrolyte fluorine concentration and PEI LiF concentrations of MTMA and LB372. **e**,**f**, TOF-SIMS 3D mapping images of LRMO PEIs after 100 cycles in MTMA (**e**) and LB372 (**f**). **g**,**h**, High-resolution transmission electron microscopy images of LRMO positrodes after 100 cycles in MTMA (**g**) and LB372 (**h**). **i**,**j**, DMT modulus distribution of the PEI formed in MTMA (**i**) and LB372 (**j**), with corresponding DMT modulus mapping images shown as insets.

electrolytes. Both MTMA- and LB372-derived PEIs exhibited high LiF content and low organic carbon content throughout their depth profile (Fig. 4a,b). LiF concentrations in the MTMA PEI at different sputtering depths were only slightly lower than that of LB372 PEI, and carbon concentrations were slightly lower in the PEI of MTMA than in LB372 PEI (Fig. 4c). Notably, even without any fluorinated solvent, the MTMA electrolyte formed a LiF-rich PEI comparable with that formed with the all-fluorinated LB372 (Fig. 4d). This demonstrates that fluorinated solvents are not necessary for construction of a chemically stable LiF-rich PEI, which is crucial for high-voltage lithium batteries[29]. Instead, provided that the competitive anodic decomposition of organic solvents is sufficiently suppressed, Li salts alone can fulfil this role. TOF-SIMS results further indicate that the MTMA PEI was slightly more organic-poor and LiF-rich compared with the PEI of LB372 (Fig. 4e,f and Supplementary Figs. 17–23). Moreover, owing to the suppression of solvent decomposition in MTMA, the resulting PEI displayed higher O, B, S, N contents derived from LiFSI and LiDFOB compared with those of MA.

High-resolution transmission electron microscopy images showed that the PEI formed in MTMA was thin and uniform (Fig. 4g). The PEI derived from LB372 was somewhat thicker and less uniform owing to gradual decomposition of fluorinated solvents on the positrode (Fig. 4h). The PEI formed in MA was the thickest, reflecting uncontrolled α-oxidation (Supplementary Fig. 24). These observations aligned well with the anodic stability trend established earlier (MTMA > LB372 > MA; Fig. 2a and Supplementary Figs. 3 and 4). Furthermore, Derjaguin–Muller–Toporov (DMT) modulus mapping confirmed that the MTMA PEI possessed superior mechanical robustness, which vital for accommodation of volume changes during cycling (Fig. 4i,j and Supplementary Fig. 25).

The increased solvent anodic stability and formation of a chemically and mechanically robust PEI in the MTMA electrolyte alleviated the aforementioned degradation mechanisms of LRMO. Blocking the α-oxidation pathway largely inhibited the generation of acidic protons upon solvent oxidation. Hence, surface structure degradation caused by acidic corrosion from the electrolyte was mitigated[32,34]. Less surface protonation was observed in MTMA as a direct result of removal of α-hydrogens (Supplementary Fig. 26). High-angle annular dark-field scanning transmission electron microscopy images revealed that LRMO cycled in MTMA retained its original layered structure

at the surface (Supplementary Fig. 27). By contrast, an irreversible phase transition was observed at the surface of LRMO cycled in MA (Supplementary Fig. 28). Further, the original Mn valence (IV) state was better preserved at the surface of MTMA-cycled particles compared with those cycled in MA (Supplementary Fig. 29). This indicated less oxygen loss at the interface (consistent with earlier DEMS results; Fig. 2e,f), which could be attributed to the stable surface structure and the robust PEI.

Mechanically, the robust PEI formed in the MTMA electrolyte better accommodated the volume changes of LRMO particles during cycling, preserving particle integrity (Supplementary Fig. 30). Minor cracks developed in LRMO particles cycled in LB372, whereas severe fractures and pulverization were observed in MA cycled LRMO. Finally, X-ray diffraction was used to assess bulk structural degradation on the basis of the ratio of two diffraction peak intensities, $I_{(003)}/I_{(104)}$, which indicates the extent of transition metal ion disorder and structural degradation in LRMO. The ratios were ordered as follows: pristine > MTMA > MA ≈ LB372 (Supplementary Fig. 31); this indicated that bulk degradation was mildest in the MTMA electrolyte and confirmed that stabilization of the surface effectively preserved the bulk lattice and enables long cycle life in Li/LRMO cells.

Characterization of SEI and Li deposition behaviours

The stability of the electrolyte towards Li metal is also important for practical cell cycling. Theoretically, replacing the α-hydrogens with electron-donating methyl groups raises the lowest unoccupied molecular orbital energy level, enhancing the cathodic stability of MTMA. Furthermore, our previous experimental work[35] showed that α-hydrogens in MA triggered severe side reactions with Li metal, whereas substituting them with inert groups (for example, methyl) greatly enhanced stability.

We ran Li/Li and Li/Cu cells with MTMA at the same current density and areal capacity with the low-loading Li/LRMO cells, that is, 0.5 mA cm^{-2} and 0.5 mAh cm^{-2} (Supplementary Fig. 32). Both cells failed quickly, in marked contrast to the >700-cycle life span of the Li/LRMO cells. This suggested that the SEI properties and Li deposition behaviour on the negatrode were strongly influenced by the presence of the positrode. When the charging cutoff voltage was adjusted, cells with the MTMA electrolyte exhibited an unusual trend: cycling stability improved substantially at higher cutoff voltages (Supplementary Fig. 33 and Supplementary Note 4). This observation was consistent with previous report indicating that high-potential positrodes can induce favourable crosstalk, wherein anions are first oxidized at the positrode, migrate to the negatrode and are subsequently reduced to form an anion-derived SEI[36]. Comparison of Li deposition morphology (Supplementary Fig. 34) and the composition of SEI on the Cu electrode in Li/Cu and Cu/LRMO cells (Supplementary Figs. 35–40 and Supplementary Note 5) further supported this theory.

Nevertheless, the electrochemical stability of the solvent remains critical to prevent solvent-related side reactions from interfering with crosstalk-driven SEI formation. In Cu/LRMO cells, both MTMA and LB372 delivered a dense and granular Li morphology, whereas MA produced a loose and dendritic morphology (Supplementary Fig. 41). We further compared the SEI on Li metal in cycled Li/LRMO cells and found that the SEI derived from MTMA was markedly more inorganic-rich, containing higher amounts of LiF and abundant salt-derived species (B, S, N), in contrast to the organic-rich SEI generated by MA decomposition (Supplementary Figs. 42–47). Combined with TOF-SIMS and DMT modulus mapping, these results confirm that the superior electrochemical stability of MTMA suppresses solvent decomposition (Supplementary Figs. 48 and 49). This allows the Li salts to fully dictate the formation of a mechanically robust, inorganic-rich SEI that supports long-term Li metal cycling under practical conditions.

Cycling performance under practical conditions

Practical high-specific-energy cells demand high positrode areal capacities, low negative-to-positive areal capacity (N/P) ratios, and low electrolyte-to-capacity (E/C) ratios. In 50-μm Li/6.0 mAh cm^{-2} LRMO coin cells, the MTMA electrolyte supported 110 stable cycles at both 4.6 V and 4.7 V, whereas the fluorinated LB372 baseline failed rapidly after 70–80 cycles (Supplementary Fig. 50). Pushing to a harsher 8.0 mAh cm^{-2} positrode areal capacity (N/P = 1.25), the 4.6-V cell with MTMA maintained 91.6% of its initial capacity after 60 cycles at 0.1 C charge/discharge, whereas LB372 failed within 10 cycles (Fig. 5a). Increasing the discharge rate to 0.3 C extended the cycle life of the MTMA cell to 90 cycles (Supplementary Fig. 51a). At a charge/discharge rate of 0.2 C/0.5 C, MTMA could still support 75 cycles with 90.1% capacity retention (Supplementary Fig. 51b). A cycle life of 73 cycles with 80.8% retention was achieved when the cutoff voltage was increased to 4.7 V (Supplementary Fig. 51c). Under more extreme conditions, full cells (10.0 mAh cm^{-2} LRMO, N/P = 1.0) with MTMA showed 93.0% capacity retention after 50 cycles at 0.1 C/0.1 C (Fig. 5b). With limited electrolyte (4.5 μl mAh^{-1}, ~4.6 g Ah^{-1} for MTMA electrolyte), the cell maintained 84.0% retention after 50 cycles at 0.1 C/0.3 C (Supplementary Fig. 52). With further reduction of the excess Li negatrode, the 5-μm Li/8.0 mAh cm^{-2} (N/P = 0.125) LRMO cell reached 77.7% retention after 50 cycles (Supplementary Fig. 51d). With limited electrolyte (4.6 g Ah^{-1}), the 5-μm Li/10.0 mAh cm^{-2} LRMO cell maintained 81.6% retention after 41 cycles (Fig. 5c). Upon scaling up, a 1.8 Ah pouch cell (8.0 mAh cm^{-2} LRMO, N/P = 1.25, E/C = 2.0 g Ah^{-1}) achieved 78 cycles with 91.3% capacity retention (Fig. 5d,e and Supplementary Table 3). Compared with state-of-the-art fluorinated electrolytes for high-voltage (≥4.4 V) LMBs[31,37–43], MTMA operated stably at much higher positrode areal capacities and lower N/P ratios (Fig. 5f).

We further constructed 7.2 Ah pouch cells to evaluate the potential application of the MTMA electrolyte in >600 Wh kg^{-1} cells. The cell with 601.8 Wh kg^{-1} could be stably cycled for 35 cycles with almost no decay in capacity or specific energy (Supplementary Figs. 53 and 54 and Supplementary Table 4). Furthermore, reducing the N/P ratio to 0.75 increased the specific energy of the 7.2 Ah cell to a maximum of 652.4 Wh kg^{-1} (Fig. 5g,h, Supplementary Fig. 55 and Supplementary Table 5). Even under such stringent conditions, the cell retained 94.5% of its capacity and 93.1% of its energy after 28 cycles. Compared with recent work on electrolyte engineering for high-specific-energy pouch cells[7,8,31,41,44–52], MTMA achieved a superior specific energy of 652.4 Wh kg^{-1} in a 4.6-V cell without any fluorinated organic solvents (Fig. 5i and Supplementary Table 6).

In addition to high-specific-energy applications, we evaluated the kinetic capability of the MTMA electrolyte for high-power scenarios, such as electric vertical take-off and landing (eVTOL) aircraft using 5.0 Ah Li/$LiNi_{0.8}Co_{0.1}Mn_{0.1}O_2$ (NCM811) cells (30 μm Li, 5.5 mAh cm^{-2} NCM811, 4.7 V upper cutoff). Subjected to a simulated eVTOL discharge protocol[42] operating between approximately 70% and 100% state of charge (Supplementary Fig. 56), the MTMA-based cells sustained this aggressive protocol for 355 cycles, with an average Coulombic efficiency of 99.92%, an average energy efficiency of 90.86% and minimal overpotential growth, before the discharge voltage dropped <2.8 V (Supplementary Fig. 57). To demonstrate this exceptional stability and rapid kinetics in a real-world application, we showed that a module assembled from four such pouch cells (Supplementary Fig. 58) successfully enabled a quadcopter unmanned aerial vehicle (UAV) through take-off, prolonged high-altitude hovering and landing in an outdoor field test at 5 °C (Supplementary Fig. 59 and Supplementary Video 1). This confirms that the MTMA-based electrolyte meets the high specific power and energy requirements for large-scale UAV batteries.

Crucially, MTMA pairs these electrochemical breakthroughs with economic viability. Preliminary cost analysis confirmed that MTMA is much cheaper than advanced fluorinated solvents and comparable in

https://doi.org/10.1038/s41557-026-02161-2

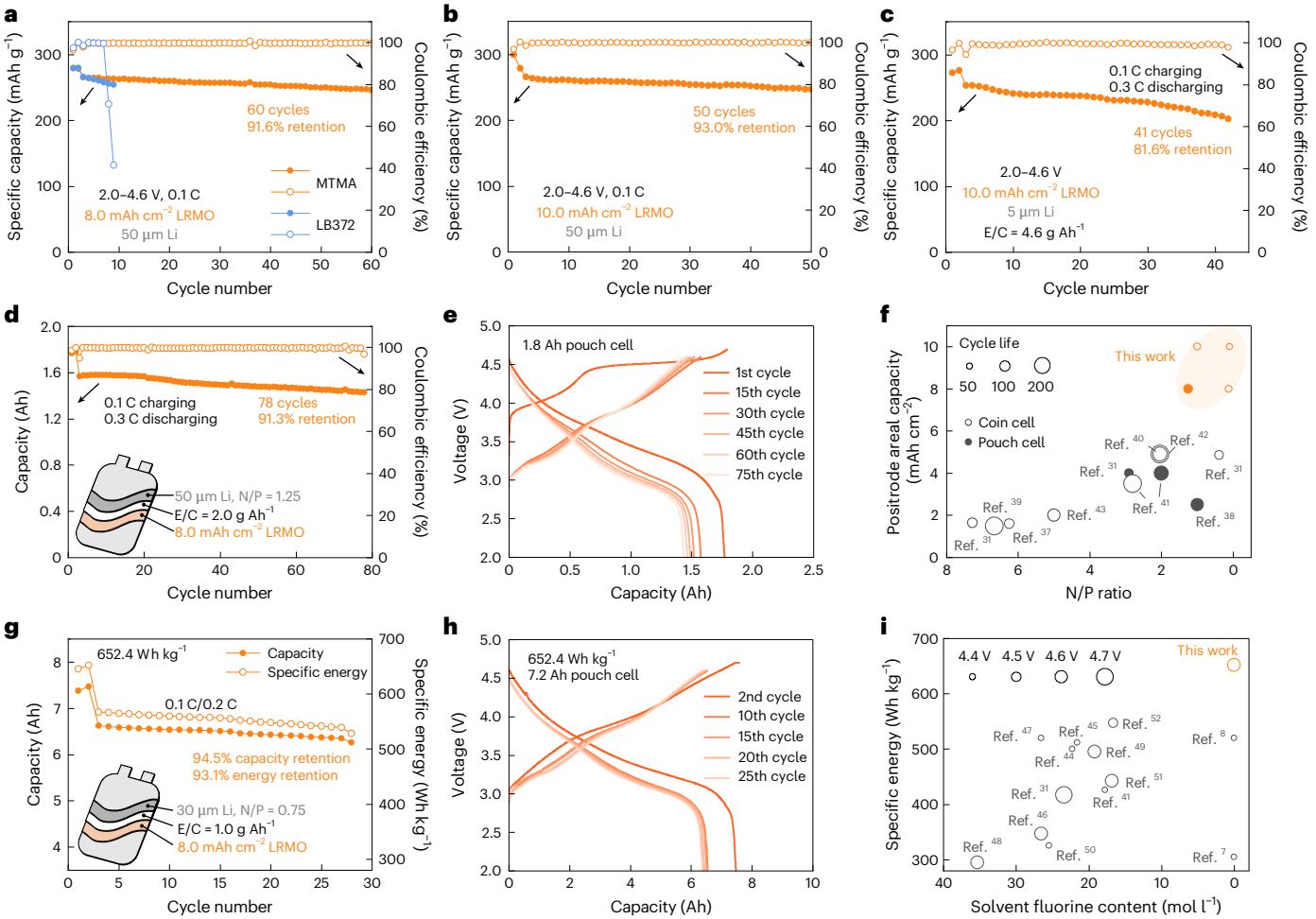

Fig. 5 | Cycling performance of high-loading Li/LRMO full cells. a–**c**, Cycling performance of Li/LRMO coin cells with N/P ratios of 1.25 (**a**), 1.0 (**b**) and 0.1 (**c**). **d**, Cycling performance of 1.8 Ah pouch cell. Inset: schematic of the pouch cell. **e**, Charge/discharge profiles of the 1.8 Ah pouch cell. **f**, Comparison of positrode areal capacity and N/P ratio between MTMA non-fluorinated electrolyte and state-of-the-art fluorinated electrolytes for high-voltage (≥4.4 V) LMBs. **g**, Cycling performance of 7.2 Ah, >650 Wh kg^{-1} pouch cell. Inset: schematic of the pouch cell. **h**, Charge/discharge profiles of the 7.2 Ah pouch cell. **i**, Comparison of specific energy and solvent fluorine content of the electrolyte in state-of-the-art high-voltage (≥4.4 V) LMBs.

cost to widely used commercial carbonates (Supplementary Fig. 60 and Supplementary Tables 7 and 8). Furthermore, as a simple, single-solvent system, MTMA provides an ideal 'clean baseline' for synergistic additive engineering, allowing interphase chemistries to be readily tailored for diverse electrode systems.

Finally, to further push the boundary of fluorine-free formulations, we evaluated an entirely fluorine-free MTMA electrolyte: $LiClO_4$ with 5.0 vol% of vinylene carbonate. The fluorine-free electrolyte delivered 78.4% capacity retention after 60 cycles in a 50-μm Li/6.0 mAh cm^{-2} LRMO cell (Supplementary Fig. 61). This confirmed that the MTMA-based electrolyte design can function even in fully fluorine-free systems, highlighting the robustness of the molecular design strategy.

Expanding the scope of the molecular design strategy beyond esters

To demonstrate the generality of our molecular design strategy, we extended our investigation to representative amides, ketones and ethers (Fig. 6a). Amides and ketones are common carbonyl-containing electrolyte candidates, and ethers were included as the α-oxidation mechanism has already been reported in previous studies[53]. We used LSV tests to evaluate the oxidative stability of conventional, α-H-containing solvents (*N*,*N*-dimethylacetamide, dimethyl ketone and tetrahydrofuran; Supplementary Fig. 1) and their α-H-free counterparts (*N*,*N*-dimethylpivalamide, di-*t*-butyl ketone (DtBK) and 1,8-cineole; Supplementary Fig. 1). Whereas $LiClO_4$ was prioritized for exploration of completely fluorine-free formulations, lithium bis(trifluoromethanesulfonyl)imide (LiTFSI) and MTMA-based solvent mixtures were used for the ketones and ethers, respectively, to overcome the poor salt solubility of DtBK and 1,8-cineole.

Across all three solvent classes, the α-H-free molecules exhibited higher oxidation onset potentials than their α-H-containing counterparts (Fig. 6b–d). Notably, calculations revealed that these α-H-free molecules possessed higher HOMO energy levels despite being more resistant to oxidation compared with their conventional counterparts (Supplementary Fig. 62 and Supplementary Note 6). This reaffirms our core hypothesis: a low HOMO energy level is not a prerequisite for high anodic stability; rather, stability is dictated by specific decomposition mechanisms. Practically, the α-H removal strategy represents an effective means of designing high-potential-stable electrolytes without relying on fluorine or electron-withdrawing substituents, enabling greener and more cost-effective battery chemistries.

Conclusion

This study identifies α-oxidation of the carbonyl group as a primary degradation pathway for carboxylate-ester-based electrolytes in high-voltage lithium batteries. On the basis of our understanding of this

https://doi.org/10.1038/s41557-026-02161-2

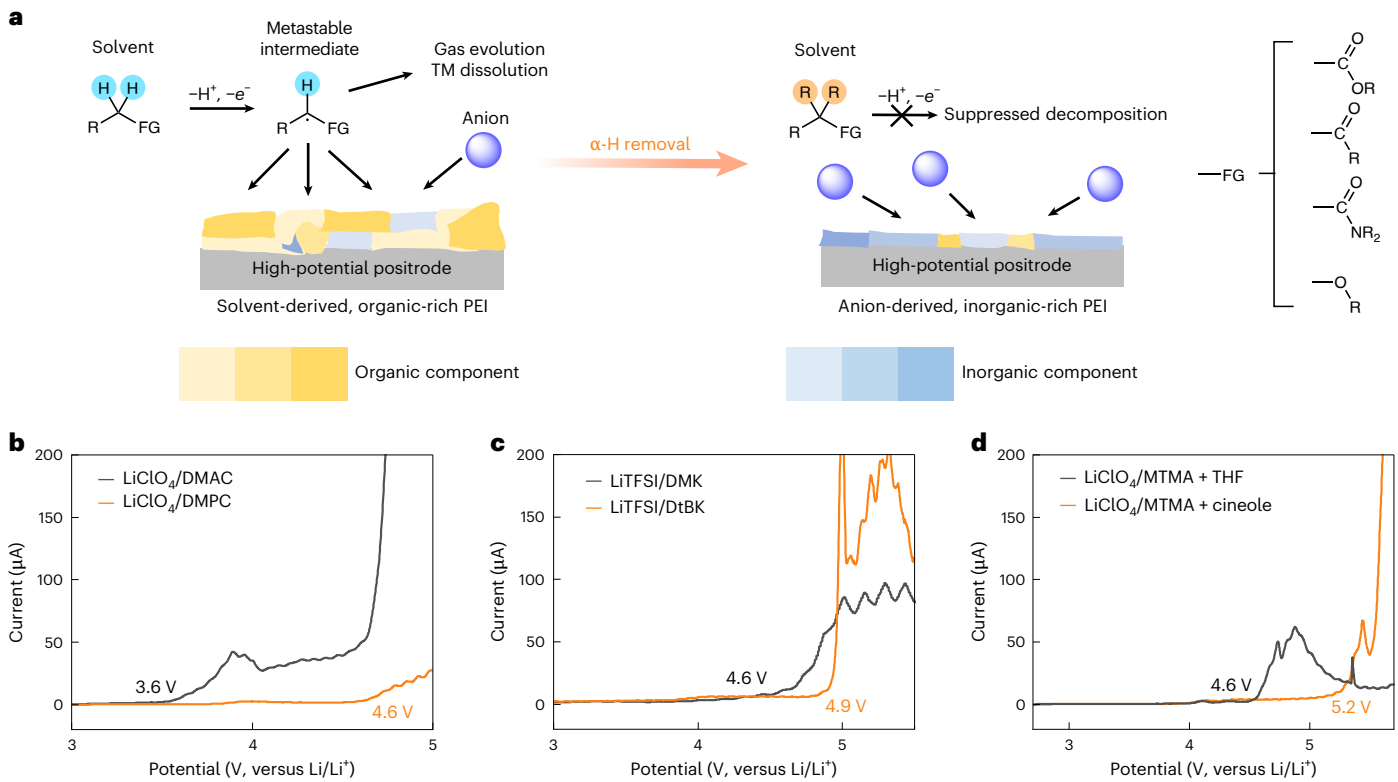

Fig. 6 | Schematic of α-H-mediated solvent oxidation on the positrode and scope of the proposed molecular design strategy. a, Schematic of solvent α-oxidation on the positrode and the corresponding molecular design strategy to address such issues. **b**–**d**, LSV results comparing conventional solvents and α-H-free solvents in amides (**b**), ketones (**c**) and ethers (**d**).

mechanism, we rationally designed a non-fluorinated solvent MTMA that strategically removes reactive α-hydrogens to block this decomposition mechanism. The resulting MTMA-based electrolyte demonstrates exceptional electrochemical stability and enables the long-term cycling of high-voltage Li/LRMO cells under stringent conditions. A 7.2 Ah Li/LRMO pouch cell delivered 652.4 Wh kg^{-1} with excellent capacity retention, whereas a fully fluorine-free formulation with $LiClO_4$ further showed broad compatibility. The extension of this α-H removal strategy to amides, ketones and ethers demonstrates its general applicability beyond carboxylate esters. This work bridges the gap between classical organic theory and electrochemical applications, highlighting how a simple molecular-level modification can redefine oxidation stability and interfacial behaviour, thereby providing a sustainable alternative to fluorinated electrolytes for high-specific-energy lithium batteries.

Online content

Any methods, additional references, Nature Portfolio reporting summaries, source data, extended data, supplementary information, acknowledgements, peer review information; details of author contributions and competing interests; and statements of data and code availability are available at https://doi.org/10.1038/s41557-026-02161-2.

References

1. Huang, X.-Y. et al. Tailoring polymer electrolyte solvation for 600 Wh kg^{-1} lithium batteries. *Nature* **646**, 343–350 (2025).
2. He, W. et al. Challenges and recent advances in high capacity Li-rich cathode materials for high energy density lithium-ion batteries. *Adv. Mater.* **33**, 2005937 (2021).
3. Cheng, X.-B. et al. A perspective on sustainable energy materials for lithium batteries. *SusMat* **1**, 38–50 (2021).
4. Fan, X. & Wang, C. High-voltage liquid electrolytes for Li batteries: progress and perspectives. *Chem. Soc. Rev.* **50**, 10486–10566 (2021).
5. Li, A.-M. et al. Methylation enables the use of fluorine-free ether electrolytes in high-voltage lithium metal batteries. *Nat. Chem.* **16**, 922–929 (2024).
6. Qiao, R. et al. Non-fluorinated electrolytes with micelle-like solvation for ultra-high-energy-density lithium metal batteries. *Chem* **11**, 102306 (2025).
7. Wang, Y. et al. Fully methylated siloxane-based electrolyte for practical lithium metal batteries. *J. Am. Chem. Soc.* **147**, 10772–10783 (2025).
8. Li, R. et al. Unified affinity paradigm for the rational design of high-efficiency lithium metal electrolytes. *Nat. Energy* **10**, 1155–1165 (2025).
9. Wang, Z. et al. An intrinsically nonflammable electrolyte for prominent-safety lithium metal batteries with high energy density and cycling stability. *Adv. Funct. Mater.* **33**, 2215065 (2023).
10. Zhang, Y. et al. Tailoring anion-enriched solvation structures in phosphate-based electrolytes for safety-enhanced lithium metal batteries. *Adv. Funct. Mater.* **35**, 2504367 (2025).
11. Wan, H., Xu, J. & Wang, C. Designing electrolytes and interphases for high-energy lithium batteries. *Nat. Rev. Chem.* **8**, 30–44 (2024).
12. Yamada, Y., Wang, J., Ko, S., Watanabe, E. & Yamada, A. Advances and issues in developing salt-concentrated battery electrolytes. *Nat. Energy* **4**, 269–280 (2019).
13. Cao, X., Jia, H., Xu, W. & Zhang, J.-G. Review—localized high-concentration electrolytes for lithium batteries. *J. Electrochem. Soc.* **168**, 010522 (2021).
14. Wang, Y. et al. Fluorination in advanced battery design. *Nat. Rev. Mater.* **9**, 119–133 (2024).
15. Vinay, B. et al. Fluorine-free electrolytes in batteries: principles, strategies, and advances. *Energy Environ. Sci.* **18**, 7326–7372 (2025).
16. Savvidou, E. K. et al. PFAS-free energy storage: investigating alternatives for lithium-ion batteries. *Environ. Sci. Technol.* **58**, 21908–21917 (2024).

17. Wackett, L. P. Nothing lasts forever: understanding microbial biodegradation of polyfluorinated compounds and perfluorinated alkyl substances. *Microb. Biotechnol.* **15**, 773–792 (2022).
18. Chong, D. P., Gritsenko, O. V. & Baerends, E. J. Interpretation of the Kohn–Sham orbital energies as approximate vertical ionization potentials. *J. Chem. Phys.* **116**, 1760–1772 (2002).
19. Safi, Z. S., Wazzan, N. & Aqel, H. Calculation of vertical and adiabatic ionization potentials for some benzaldehydes using hybrid DFT, multilevel G3B3 and MP2 methods. *Chem. Phys. Lett.* **791**, 139349 (2022).
20. Sowndarya, S. V., St, S., John, P. C. & Paton, R. S. A quantitative metric for organic radical stability and persistence using thermodynamic and kinetic features. *Chem. Sci.* **12**, 13158–13166 (2021).
21. Borodin, O. Challenges with prediction of battery electrolyte electrochemical stability window and guiding the electrode–electrolyte stabilization. *Curr. Opin. Electrochem.* **13**, 86–93 (2019).
22. Peljo, P. & Girault, H. H. Electrochemical potential window of battery electrolytes: the HOMO–LUMO misconception. *Energy Environ. Sci.* **11**, 2306–2309 (2018).
23. Liang, S., Xu, K., Zeng, C.-C., Tian, H.-Y. & Sun, B.-G. Recent advances in the electrochemical α-C–H bond functionalization of carbonyl compounds. *Adv. Synth. Catal.* **360**, 4266–4292 (2018).
24. Lin, M. et al. Initial stages of oxidation reactions of ethylene carbonate and fluoroethylene carbonate on Li_xCoO_2 surfaces: a DFT study. *J. Electrochem. Soc.* **168**, 050505 (2021).
25. Xia, L. et al. Oxidation decomposition mechanism of fluoroethylene carbonate-based electrolytes for high-voltage lithium ion batteries: a DFT calculation and experimental study. *ChemistrySelect* **2**, 7353–7361 (2017).
26. Wan, G. et al. Solvent-mediated oxide hydrogenation in layered cathodes. *Science* **385**, 1230–1236 (2024).
27. Rinkel, B. L. D., Hall, D. S., Temprano, I. & Grey, C. P. Electrolyte oxidation pathways in lithium-ion batteries. *J. Am. Chem. Soc.* **142**, 15058–15074 (2020).
28. Xu, K., Ding, S. P. & Jow, T. R. Toward reliable values of electrochemical stability limits for electrolytes. *J. Electrochem. Soc.* **146**, 4172 (1999).
29. Fan, X. et al. Non-flammable electrolyte enables Li-metal batteries with aggressive cathode chemistries. *Nat. Nanotechnol.* **13**, 715–722 (2018).
30. Zhang, K. et al. Sulfuration of Li-rich Mn-based cathode materials for multianionic redox and stabilized coordination environment. *Adv. Mater.* **34**, 2109564 (2022).
31. Xue, W. et al. Ultra-high-voltage Ni-rich layered cathodes in practical Li metal batteries enabled by a sulfonamide-based electrolyte. *Nat. Energy* **6**, 495–505 (2021).
32. Chen, H., Xia, X. & Ma, J. Comprehensive review of Li-rich Mn-based layered oxide cathode materials for lithium-ion batteries: theories, challenges, strategies and perspectives. *ChemSusChem* **17**, e202401120 (2024).
33. Yan, P. et al. Injection of oxygen vacancies in the bulk lattice of layered cathodes. *Nat. Nanotechnol.* **14**, 602–608 (2019).
34. Zheng, J. et al. Corrosion/fragmentation of layered composite cathode and related capacity/voltage fading during cycling process. *Nano Lett.* **13**, 3824–3830 (2013).
35. Yang, Y. et al. Removing α-H in carboxylate-based electrolytes for stable lithium metal batteries. *Angew. Chem. Int. Ed.* **64**, e202503616 (2025).
36. Tan, S. et al. Unravelling the convoluted and dynamic interphasial mechanisms on Li metal anodes. *Nat. Nanotechnol.* **18**, 243–249 (2023).
37. Yuan, X. et al. Bi-affinity electrolyte optimizing high-voltage lithium-rich manganese oxide battery via interface modulation strategy. *Angew. Chem. Int. Ed.* **62**, e202304121 (2023).
38. Wang, H. et al. An entanglement association polymer electrolyte for Li-metal batteries. *Nat. Commun.* **15**, 2500 (2024).
39. Cao, X. et al. Monolithic solid–electrolyte interphases formed in fluorinated orthoformate-based electrolytes minimize Li depletion and pulverization. *Nat. Energy* **4**, 796–805 (2019).
40. Yu, Z. et al. Rational solvent molecule tuning for high-performance lithium metal battery electrolytes. *Nat. Energy* **7**, 94–106 (2022).
41. Zhang, G. et al. A monofluoride ether-based electrolyte solution for fast-charging and low-temperature non-aqueous lithium metal batteries. *Nat. Commun.* **14**, 1081 (2023).
42. Choi, I. R. et al. Asymmetric ether solvents for high-rate lithium metal batteries. *Nat. Energy* **10**, 365–379 (2025).
43. Xiao, P. et al. A nonflammable electrolyte for ultrahigh-voltage (4.8 V-class) Li||NCM811 cells with a wide temperature range of 100 °C. *Energy Environ. Sci.* **15**, 2435–2444 (2022).
44. Zhang, S. et al. Oscillatory solvation chemistry for a 500 Wh kg^{-1} Li-metal pouch cell. *Nat. Energy* **9**, 1285–1296 (2024).
45. Zhang, G. et al. High-energy and fast-charging lithium metal batteries enabled by tuning Li^+-solvation via electron-withdrawing and lithiophobicity functionality. *Nat. Commun.* **16**, 4722 (2025).
46. Peng, X., Wang, T., Liu, B., Li, Y. & Zhao, T. A solvent molecule reconstruction strategy enabling a high-voltage ether-based electrolyte. *Energy Environ. Sci.* **15**, 5350–5361 (2022).
47. Jie, Y. et al. Towards long-life 500 Wh kg^{-1} lithium metal pouch cells via compact ion-pair aggregate electrolytes. *Nat. Energy* **9**, 987–998 (2024).
48. Wu, S. et al. Uncovering the crucial role of chelating structures in cyano-alkyl-phosphate electrolytes for high-voltage lithium metal batteries. *J. Am. Chem. Soc.* **146**, 28770–28782 (2024).
49. Lu, Y. et al. Tuning the Li^+ solvation structure by a "bulky coordinating" strategy enables nonflammable electrolyte for ultrahigh voltage lithium metal batteries. *ACS Nano* **17**, 9586–9599 (2023).
50. Yu, Z. et al. Molecular design for electrolyte solvents enabling energy-dense and long-cycling lithium metal batteries. *Nat. Energy* **5**, 526–533 (2020).
51. Mao, M. et al. Anion-enrichment interface enables high-voltage anode-free lithium metal batteries. *Nat. Commun.* **14**, 1082 (2023).
52. Ji, H. et al. Liquid–liquid interfacial tension stabilized Li-metal batteries. *Nature* **643**, 1255–1262 (2025).
53. Nie, K. et al. Increasing poly(ethylene oxide) stability to 4.5 V by surface coating of the cathode. *ACS Energy Lett.* **5**, 826–832 (2020).

Publisher's note Springer Nature remains neutral with regard to jurisdictional claims in published maps and institutional affiliations.

Springer Nature or its licensor (e.g. a society or other partner) holds exclusive rights to this article under a publishing agreement with the author(s) or other rightsholder(s); author self-archiving of the accepted manuscript version of this article is solely governed by the terms of such publishing agreement and applicable law.

© The Author(s), under exclusive licence to Springer Nature Limited 2026

[1]Beijing Key Laboratory of Complex Solid-State Batteries, Department of Chemical Engineering, Tsinghua University, Beijing, China. [2]School of Interdisciplinary Science, Beijing Institute of Technology, Beijing, China. [3]AI Solid-State Battery Innovation Center, Yibin, China. [4]School of Chemistry, Xi'an Jiaotong University, Xi'an, China. [5]Engineering Research Center of Energy Storage Materials and Devices, Ministry of Education, Engineering Research Center of Energy Storage Materials and Chemistry, Xi'an, China. [6]Center of Basic Molecular Science, Department of Chemistry, Tsinghua University, Beijing, China. [7]State Key Laboratory of Heavy Oil Processing, College of Chemical Engineering and Environment, China University of Petroleum, Beijing, China. [8]State Key Laboratory of Chemical Engineering and Low-Carbon Technology, Tsinghua University, Beijing, China. [9]Shanxi Research Institute for Clean Energy, Tsinghua University, Taiyuan, China. [10]These authors contributed equally: Yu-Xin Huang, Yi Yang. ✉e-mail: zcz@mail.tsinghua.edu.cn; zhang-qiang@mails.tsinghua.edu.cn

Methods

Chemicals and materials

Thick Li foil (diameter of 16.0 mm and thickness of 600 µm) and thin Li foil (thickness 50 µm) were obtained from China Energy Lithium. High-loading (6.0, 8.0, 10.0 mAh cm^{-2}), single-sided LRMO positrodes were prepared with an active material ratio of 94.7 wt%; 8.0 mAh cm^{-2} double-sided LRMO positrodes were prepared with 97.0 wt% LRMO; and 5.5 mAh cm^{-2} $LiNi_{0.8}Co_{0.1}Mn_{0.1}O_2$ (NCM811) positrodes were prepared with 96.5 wt% active material. The 50-µm Li negatrodes for coin cells were prepared by calendering the Li foil on to 6-µm Cu foil then punched into round discs with 15 mm diameter (d = 15 mm). The 5-µm Li negatrodes were also punched into d = 15 mm discs. For the low-loading (0.5 mAh cm^{-2}) positive electrode (positrode), the positrode slurry was prepared by mixing 80.0 wt% LRMO, 10.0 wt% Super P and 10.0 wt% polyvinylidene difluoride (Alfa Aesar) in *N*-methyl-2-pyrrolidone (Aladdin). The positrodes were obtained by coating the slurry on to carbon-coated aluminium foil with a knife coater and dried in a vacuum oven at 80 °C for 12 h. The 0.5, 6.0 and 8.0 mAh cm^{-2} positrodes were punched into d = 10 mm discs before fabrication of coin cells or use in mechanistic studies. The 10.0 mAh cm^{-2} positrodes were cut into both 10-mm- and 13-mm-diameter discs for coin cells. Polyethylene (PE) separators (32 µm, 25 µm, 16 µm) were purchased from Asahi Kasei Technosystem. Battery-grade solvents (vinylene carbonate), Li salts ($LiPF_6$, LiFSI, LiDFOB, LiTFSI, $LiClO_4$) and electrolyte (LB372: 1.0 M $LiPF_6$, 0.02 M LiDFOB, FEC/3,3,3-fluoroethylmethyl carbonate/1,1,2,2-tetrafluoroethyl-2,2,2-trifluoroethyl ether (2/6/2 by weight)) were purchased from Do. Do. Chem. The 3-Å molecular sieve was purchased from Sigma-Aldrich and activated at 180 °C in a vacuum oven for 24 h before use. Methanol-d_1, methanol-d_4, acetic acid-d_1, acetic acid-d_4 and concentrated D_2SO_4 (96–98% in D_2O) were purchased from Energy Chemical. MA (anhydrous), MTMA, *t*-butyl acetate and *n*-decane were purchased from J&K Scientific. The two partially deuterated MA were synthesized according to the methods reported by Winnik et al.[54]. All solvents that were not battery grade or anhydrous were dried with the 3-Å molecular sieve (1 g sieve for every 10 ml solvent) for at least 24 h before use. Al-clad positrode cases (CR2025, Canrd Technology), aluminium foils, copper foils and carbon-coated aluminium foils were dried in an oven at 60 °C for at least 24 h before use. Carbon-coated aluminium foils and copper foils were punched into d = 13 mm and d = 15 mm discs, respectively.

Electrolyte preparation

All the concentrations mentioned in this work were calculated on the basis of the volume of solvents rather than the total volume of the whole solution. For example, to prepare 1.2 M LiFSI + 0.4 M LiDFOB in MTMA, 0.2244 g LiFSI (1.2 mmol) and 0.0576 g LiDFOB (0.4 mmol) were dissolved in 1,000 µl MTMA. After the salt had been fully dissolved, the electrolyte was filtered through a PTFE syringe filter with a pore size of 0.22 µm to remove dust and any other insoluble impurities. Then, ~0.2 wt% of 3 Å molecular sieve was added to the filtered electrolyte to further remove residual water.

Cell assembly

Coin cells were assembled in an Ar-filled glovebox with <0.1 ppm H_2O and <0.1 ppm O_2. The default assembly procedure involved placing or adding the following parts sequentially: 2025 positrode case, positrode, 40 µl electrolyte, separator, 40 µl electrolyte, negatrode, spacer, spring, 2025 negatrode case. For cells that were operated over 4.0 V versus Li/Li^+ (for example, Li/LRMO full cells, Li/carbon-coated Al for LSV), Al-clad positrode cases were used; otherwise, regular stainless steel positrode cases were used. For coin cells that used limited electrolyte (4.5 µl mAh^{-1}), d = 13 mm, 10.0 mAh cm^{-2} positrodes were used, and only 30 µl + 30 µl electrolyte was added stepwise.

Li/LRMO and Li/NCM811 pouch cells (7.0 × 4.0 cm^2) were assembled in a dry room at a dew point of −60 °C. The Li negatrode was prepared by calendering 50-µm- or 30-µm-thick Li foils on copper current collectors. First, the positrodes and Li negatrodes were stacked layer-by-layer with a PE separator in a repeating negatrode|PE|positrode|PE|negatrode | … sequence, followed by packing in an aluminium–plastic film package. The pouch cell was subsequently hermetically sealed under vacuum. Finally, after being allowed to rest for at least 6 h at 25 °C, the pouch cell was subjected to electrochemical testing.

H-cells were assembled by clamping the two chambers together with three 32-µm PE separators at the junction. Then, 5 ml of electrolyte was then added to each of the negatrode and positrode chambers. Finally, the electrodes were inserted, and parafilm was further used to ensure air tightness.

Electrochemical measurement

All cycling performances of coin cells were measured on a LAND multichannel battery testing system (Wuhan LAND Electronics) at 25 °C. For all Li/LRMO cells, 1.0 C = 250 mA g^{-1}; the cycle voltage ranges and charge/discharge rates after activation are provided in the main text and figures. The coin cells were all charged using the constant current (CC) method. Low-loading Li/LRMO cells were first cycled in a voltage range of 2.0–4.6 V or 2.0–4.7 V at 0.1 C/0.1 C, 0.2 C/0.2 C, 0.5 C/0.5 C for 1 cycle each for activation of the cells, and then at 1.0 C/1.0 C for subsequent cycles. Coin cells with 6.0 mAh cm^{-2} positrodes were activated by cycling at 0.05 C/0.05 C and 0.1 C/0.1 C for 1 cycle each, followed by 0.2 C/0.5 C long cycling. Coin cells using 8.0 and 10.0 mAh cm^{-2} positrodes were activated by 2 cycles of 0.05 C/0.05 C charge/discharge, followed by long cycling at various rates (provided in the main text and figures). Li/LRMO pouch cells were cycled under 1.0 MPa external pressure. The 1.8 Ah cell was activated at 0.05 C/0.05 C between 2.0 V and 4.7 V using CC charging for 2 cycles, then cycled at 0.1 C/0.3 C between 2.0 V and 4.6 V under CC mode. The 7.2 Ah cells were activated at 0.05 C/0.05 C between 2.0 V and 4.7 V using CC-constant voltage (CC-CV) charging for 2 cycles, with the CV step at 4.7 V terminated once the current dropped below 0.025 C. Subsequently, the cells were cycled at 0.1 C/0.2 C between 2.0 V and 4.6 V under CC charging. The Li/NCM85 coin cells were cycled between either 3.0 V and 4.3 V or between 3.0 V and 4.6 V, with 2 cycles of 0.05 C/0.05 C activation followed by 0.1 C/0.1 C long cycling (1 C = 190 mA g^{-1}). For the eVTOL protocol cycling, the 5.0 Ah Li/NCM811 pouch cells were activated at 0.05 C/0.05 C between 3.0 and 4.7 V using CC charging for 1 cycle. Then, the cells were charged at 0.15 C using CC-CV charging, with the CV step at 4.7 V terminated once the current dropped below 0.075 C, followed by eVTOL discharge (3.0 C for 30 s, 1.3 C for 120 s, 0.9 C for 1020 s, 0.3 C for 120 s, and finally 3.0 C for 30 s) every cycle (1 C = 190 mA g^{-1}). For the UAV test flight, the 5.0 Ah Li/NCM811 pouch cells were charged separately at 0.05 C to 4.7 V. Four such cells were then assembled into a battery module and subjected to the UAV experiment.

Electrochemical characterizations were carried out on an electrochemical station (Solartron EnergyLab XM). The in situ EIS during 0.1 C charging/discharging of lithium batteries was tested in a frequency from 1 MHz to 0.1 Hz at an amplitude of 10 mV. Galvanostatic intermittent titration technique measurements were conducted after 100 cycles (MTMA, LB372) or 50 cycles (MA) of 1.0 C cycling between 2.0 V and 4.7 V. The cells were first subjected to 1 cycle at 0.1 C/0.1 C to allow them to recover capacity 'loss' due to polarization at a high charge/discharge rate. Next, the galvanostatic intermittent titration technique was conducted by repeating a titration step at 0.1 C of 30 min and a relaxation step of 30 min between 2.0 V and 4.7 V. To determine the oxidation potentials of solvents, we used the default LSV setup with an Li/carbon-coated aluminium coin cell and scanned from open circuit potential to 6.0 V at a scan rate of 0.1 mV s^{-1}. For dimethyl ketone and DtBK, LiTFSI was used owing to the limited solubility of other Li salts in DtBK. To avoid LiTFSI-related corrosion, LSV was conducted in an H-cell with a platinum working electrode, following the same electrochemical protocol as the default setup. The leak current tests

of different electrolytes in 4.8-V Li/LRMO cells were carried out by first charging the 600-µm Li/6.0 mAh cm^{-2} LRMO cells to 4.8 V at 0.1 C, then holding at 4.8 V for 10 h.

Material characterization

To analyse the electrolyte composition after oxidation on LRMO positrode, we assembled an H-cell using 600 µm Li, 6.0 mAh cm^{-2} LRMO, and either $LiPF_6$/MA or $LiPF_6$/MTMA electrolyte. The cell was anodically scanned to 4.8 V at 0.04 mV s^{-1}. Afterwards, 250 µl of the solution in the LRMO chamber was collected for transition metal dissolution measurements using inductively coupled plasma mass spectrometry (Agilent 5110). Then, 25 µl of the solution in the LRMO chamber was diluted in DMSO-d_6 and analysed by nuclear magnetic resonance (NMR) on a Bruker AVANCE III HD 400 (^{1}H at 400 MHz, ^{19}F at 376 MHz). For ^{1}H NMR, solvent suppression was used to suppress MA or MTMA signals to enhance the signal-to-noise ratio of trace species such as HF in the electrolytes. For the NMR control experiment, LSV was omitted; all other protocols were identical to those used in the oxidized case. To quantify the amounts of H_2O and peroxide produced by solvent oxidation with LRMO, 600-µm Li/6.0 mAh cm^{-2} LRMO coin cells were assembled, charged to 4.7 V and held at 4.7 V for 12 h. The cells were then disassembled, and the fully charged LRMO positrodes were removed and washed with MA or MTMA solvent (depending on which solvent's oxidation was being studied). Two fully charged LRMO positrodes were immersed in 500 µl of $LiPF_6$/MA or $LiPF_6$/MTMA electrolyte in dried vials. After 24 h of oxidation, the solution was analysed with a Coulometric Karl Fischer titrator (Mettler Toledo, C20S) and a peroxide strip (Supelco, MQuant 1.10011). DEMS (LingLu QAS 100 Li) was employed to probe gaseous products of solvent oxidation. Swagelok-type cells made in-house with 600-µm Li/10.0 mAh cm^{-2} LRMO were assembled for DEMS experiments. High-purity Ar at a speed of 1.2 ml min^{-1} was used as the carrier gas upon cycling. The Swagelok-type cells were charged at 0.1 C to 4.8 V.

Before surface characterizations, the cycled electrodes were rinsed with the same solvent used in the corresponding electrolyte to remove residual Li salts. The electrodes were then left to dry in a glovebox and later transferred for surface characterization. The morphologies of the deposited Li and LRMO positrode after cycling were examined using a scanning electron microscope (ZEISS GeminiSEM 300, 3.0 kV). High-resolution transmission electron microscopy of the surface structure of the cycled LRMO positrode was carried out with a JEOL 2100 Plus transmission electron microscope (120 kV), equipped with an Elsa 698.STP cooling system. The atomic-arrangement images of cycled LRMO positrode were obtained using high-angle annular dark-field scanning transmission electron microscopy with a Cs-corrected scanning transmission electron microscope (FEI Titan Cubed Themis G2 300) operated at 300 kV.

The SEI and PEI compositions of the Li/LRMO electrodes after cycling were analysed via X-ray photoelectron spectroscopy (AXIS Supra+, Kratos Analytical) with monochromated Al K_α radiation as the X-ray source. The depth profiles were acquired via Ar^+ sputtering at 2 kV for 0, 15, 30 and 45 s. The C 1*s* peak at 284.8 eV was used as the reference for all binding energies. TOF-SIMS (PHI nano ToF II) was employed to explore SEI/PEI composition on electrodes. For the H/D isotope TOF-SIMS experiments in Fig. 2b,c, a different electrode cleaning method was used before characterization. After cell disassembly, the electrodes were directly vacuum-dried in the glovebox antechamber for at least 10 min to remove residual solvent. Solvent rinsing was intentionally omitted from this experiment to prevent any possible surface H-D exchange with the washing solvent. Residual Li salts were not expected to affect the measured surface H/D ratio. X-ray diffraction measurements of the positrodes were performed on a Rigaku MiniFlex 600. Atomic force microscopy (Bruker Dimension Icon) was used to investigate the mechanical properties of the SEI and PEI on cycled Li metal and LRMO.

Computational details

DFT calculations of the potentials of possible redox pairs in MA and MTMA oxidation were performed in Gaussian (G16)[55] with the M06-2X[56] functional and the 6-311+g(d,p) basis set. A solvation model based on density (SMD)[57] and parameters for MA (eps = 6.8615, epsinf = 1.8534) were used. Frequency analysis was conducted to ensure the ground state of molecular structures and to obtain thermal corrections to free energies. Oxidation potentials were computed according to the Nernst equation:

$$E = \frac{\Delta G(S \rightarrow S^{ox})}{nF} - 1.4\ \mathrm{V}$$

where the numerator is the free energy difference between the oxidized species and the neutral species, and the denominator is the product of Faraday's constant and the number of electrons lost in the oxidation (always 1 in this case); 1.4 V was subtracted to shift the computed potential to the Li^+/Li scale.

The HOMO energy levels of solvents were calculated with the B3LYP[58] functional and the 6-311g(d,p) basis set in gas phase.

Data availability

Data supporting the findings of this study are available from the corresponding authors upon request. Source data are provided with this paper.

References

54. Winnik, M. A. & Stoute, V. A. A simple preparation of the isotopically substituted methyl acetates. *J. Label. Compd.* **11**, 609–612 (1975).
55. Frisch, M.J. et al. Gaussian 16, Revision C. 01 (Gaussian, 2016).
56. Zhao, Y. & Truhlar, D. G. The M06 suite of density functionals for main group thermochemistry, thermochemical kinetics, noncovalent interactions, excited states, and transition elements: two new functionals and systematic testing of four M06-class functionals and 12 other functionals. *Theor. Chem. Acc.* **120**, 215–241 (2008).
57. Marenich, A. V., Cramer, C. J. & Truhlar, D. G. Universal solvation model based on solute electron density and on a continuum model of the solvent defined by the bulk dielectric constant and atomic surface tensions. *J. Phys. Chem. B* **113**, 6378–6396 (2009).
58. Stephens, P. J., Devlin, F. J., Chabalowski, C. F. & Frisch, M. J. Ab initio calculation of vibrational absorption and circular dichroism spectra using density functional force fields. *J. Phys. Chem.* **98**, 11623–11627 (1994).

Acknowledgements

We acknowledge support from Tsinghua National Laboratory for Information Science and Technology for theoretical calculations. This work was supported by the Fundamental and Interdisciplinary Disciplines Breakthrough Plan of the Ministry of Education of China (JYB2025XDXM304), Beijing Municipal Natural Science Foundation (L243019, L247015 and L233004), National Natural Science Foundation of China (22579099, 22425901, 22393900, 22308190, T2322015 and 21825501), the Xplorer Prize, Science Foundation of China University of Petroleum Beijing (No. 2462025YJRC021) and the Tsinghua University Initiative Scientific Research Program. Y.-X.H., Z.-Y.J. and Y.-F.T. acknowledge the Tsinghua Xuetang Talents Program of Tsinghua University, and P.X. and W.-J.K. acknowledge the Shuimu Tsinghua Scholar Program of Tsinghua University.

Author contributions

Y.-X.H., Y.Y., C.-Z.Z. and Q.Z. conceived the idea and designed the experiments. Y.-X.H. and Y.Y. performed the material characterizations

and electrochemical measurements in coin cells with assistance from P.X., Z.-Z.Q., X.-Y.Z., Z.-Y.S., X.-Y.H., W.-J.K. and K.Z., and all of them helped with discussion. Z.-Y.J., Y.-X.H. and X.C. conducted DFT calculations. Y.-F.L. prepared and tested the pouch cells. Y.Y. and Y.-F.L. conducted the UAV experiments. Y.-F.T. purified the deuterated MA and assisted with NMR experiments. Y.-X.H., Y.Y., C.-Z.Z. and Q.Z. analysed the data and prepared the paper with contributions from all authors.

Competing interests

Q.Z., Y.-X.H., P.X., C.-Z.Z. and Y.Y. declare that this work has been filed as Chinese Patent Application No. CN118738566A. The other authors declare no competing interests.

Additional information

Supplementary information The online version contains supplementary material available at https://doi.org/10.1038/s41557-026-02161-2.

Correspondence and requests for materials should be addressed to Chen-Zi Zhao or Qiang Zhang.

Peer review information *Nature Chemistry* thanks George Chen and the other, anonymous, reviewer(s) for their contribution to the peer review of this work.

Reprints and permissions information is available at www.nature.com/reprints.